

# Water Resources Research

## RESEARCH ARTICLE

10.1029/2022WR032861

### Key Points:

- Lake seiche induced oscillatory flow is responsible for the turbulent structures in two stratified and low energetic lakes
- Effect of bubble plume is limited on turbulent structures in the bottom boundary layer
- Shear velocity, turbulent Batchelor length, and turbulent integral time are correlated with oxygen flux at the sediment-water interface

### Supporting Information:

Supporting Information may be found in the online version of this article.

### Correspondence to:

B. Wang,  
[wangbinb@missouri.edu](mailto:wangbinb@missouri.edu)

### Citation:

Wang, B., Rezvani, M., Bierlein, K. A., Bryant, L. D., Little, J. C., Wüest, A., & Socolofsky, S. A. (2023). Effects of bubble plumes on lake dynamics, near-bottom turbulence, and transfer of dissolved oxygen at the sediment-water interface. *Water Resources Research*, 59, e2022WR032861. <https://doi.org/10.1029/2022WR032861>

Received 21 MAY 2022  
Accepted 21 JUL 2023

### Author Contributions:

**Conceptualization:** John C. Little, Alfred Wüest, Scott A. Socolofsky  
**Data curation:** Maryam Rezvani, Kevin A. Bierlein, Lee D. Bryant  
**Formal analysis:** Binbin Wang  
**Funding acquisition:** Scott A. Socolofsky  
**Investigation:** Binbin Wang, Maryam Rezvani, Kevin A. Bierlein, Lee D. Bryant  
**Methodology:** John C. Little, Alfred Wüest, Scott A. Socolofsky  
**Visualization:** Binbin Wang  
**Writing – original draft:** Binbin Wang  
**Writing – review & editing:** Binbin Wang, John C. Little, Alfred Wüest, Scott A. Socolofsky

## Effects of Bubble Plumes on Lake Dynamics, Near-Bottom Turbulence, and Transfer of Dissolved Oxygen at the Sediment-Water Interface

Binbin Wang<sup>1</sup> , Maryam Rezvani<sup>2</sup> , Kevin A. Bierlein<sup>3</sup>, Lee D. Bryant<sup>4</sup>, John C. Little<sup>5</sup> , Alfred Wüest<sup>6,7</sup> , and Scott A. Socolofsky<sup>8</sup> 

<sup>1</sup>Department of Civil and Environmental Engineering, University of Missouri, Columbia, MO, USA, <sup>2</sup>Autodesk, Walnut Creek, CA, USA, <sup>3</sup>Hydros Consulting Inc., Boulder, CO, USA, <sup>4</sup>Department of Architecture and Civil Engineering, University of Bath, Bath, UK, <sup>5</sup>Department of Civil and Environmental Engineering, Virginia Tech, Blacksburg, VA, USA, <sup>6</sup>Physics of Aquatic Systems Laboratory (APHYS)-Margaretha Kamprad Chair, École Polytechnique Fédérale de Lausanne, Lausanne, Switzerland, <sup>7</sup>Aquatic Physics, Department of Surface Waters – Research and Management, Eawag, Swiss Federal Institute of Aquatic Science and Technology, Kastanienbaum, Switzerland, <sup>8</sup>Department of Civil and Environmental Engineering, Texas A&M University, College Station, TX, USA

**Abstract** We quantify the lake dynamics, near-bottom turbulence, flux of dissolved oxygen (DO) across the sediment-water interface (SWI) and their interactions during oxygenation in two lakes. Field observations show that the lake dynamics were modified by the bubble plumes, showing enhanced mixing in the near-field of the plumes. The interaction of the bubble-induced flow with the internal density structure resulted in downwelling of warm water into the hypolimnion in the far-field of the plumes. Within the bottom boundary layer (BBL), both lakes show weak oscillating flows primarily induced by seiche. The vertical profile of mean velocity within 0.4 m above the bed follows a logarithmic scaling. One lake shows a larger drag coefficient than those in stationary BBLs, where the classic law-of-the-wall is valid. The injection of oxygen elevated the water column DO and hence, altered the DO flux across the SWI. The gas transfer velocity is driven by turbulence and is correlated with the bottom shear velocity. The thickness of the diffusive boundary layer was found to be consistent with the Batchelor length scale. The dynamics of the surface renewal time follow a log-normal distribution, and the turbulent integral time scale is comparable to the surface renewal time. The analyses suggest that the effect of bubble plumes on the BBL turbulence is limited and that the canonical scales of turbulence emerge for the time-average statistics, validating the turbulence scaling of gas transfer velocity in low-energy lakes.

## 1. Introduction

In freshwater lakes, biodegradation of organic matter mostly occurs on and within the sediments, resulting in consumption of dissolved oxygen (DO) and a downward flux of DO from the hypolimnion into the sediments across the sediment-water interface (SWI) (Lorke et al., 2003). The rate of oxygen utilization in the sediments is critical to the mass balance of DO in the water column and influences the vertical distribution of DO in the water. Low DO in the bottom boundary layer (BBL) of the water column and in the sediments also affects the release of reduced chemical species to the lake from the sediments, hence, affecting the water quality in the hypolimnion (Beutel & Horne, 1999; Müller et al., 2012). Together, the biodegradation of organic matter and the oxygen mass flux at the SWI are recognized as the two primary driving forces responsible for hypolimnetic DO depletion during the stratified, productive season of most lakes (Müller et al., 2012).

To restore DO levels and hence, improve the ecosystem of lakes, artificial aeration (i.e., injection of air) and oxygenation (i.e., injection of pure oxygen) using bubble plumes have been widely used (e.g., Beutel & Horne, 1999; McGinnis et al., 2004; Singleton & Little, 2006; Wüest et al., 1992). Bubble plumes have been shown to strongly modify the thermal structure and the DO at mid-water depths in the near-field of bubble plumes (McGinnis et al., 2004). Bubble plumes also have the potential to influence far-field lake dynamics when interacting with lake internal motions (McGinnis et al., 2004). However, it remains unclear whether an oxygenation bubble plume can effectively alter the turbulence within the BBL that is not in the direct entrainment region of the bubble plume. Although oxygenation bubble plumes are designed to cause minimal mixing of the hypolimnion, past studies have shown links between oxygen injection and increased consumption of DO at the SWI. This is

primarily linked to two main processes: (a) the larger DO gradient between the water column and sediments because of the elevated DO in the water column, and (b) alteration of the turbulence in the BBL by currents induced by the bubble plume (Brand et al., 2009; Bryant et al., 2010).

In deep lakes, currents in the BBL are usually weak. In such low-energy environments, the BBL is expected to be restricted to a limited height above the lake bottom, typically one or a few meters (Troy et al., 2016). Large-scale lake seiche interacts with the shear flow close the lake bottom, which may further limit the thickness of the BBL where logarithmic profiles of velocity are expected (Lorke et al., 2002). Therefore, the BBL flow structure depends on the overall flow characteristics and the overlying stratification and internal motion. Even within a low-energy boundary layer, the logarithmic profile of velocity is widely observed, and the law-of-the-wall scaling seems to be valid for predicting turbulence parameters including turbulent kinetic energy (TKE) and the dissipation rate of TKE (Troy et al., 2016; Valipour et al., 2015). The law-of-the-wall hypothesizes that the turbulent shear stress ( $\tau_t$ ) in the inertial sublayer of a boundary layer is approximately the bed shear stress ( $\tau_0$ ), hence, that the shear velocity  $u_* = \sqrt{\tau_0/\rho}$  can be obtained from the turbulent shear stress profile. Here, we test the law-of-the-wall scaling in the BBL of two oxygenated lakes to determine whether the structure of the turbulence is affected by the bubble plumes.

Turbulence in the BBL affects the gas transfer at the lake bottom by intermittently flushing the diffusive boundary layer at the SWI. Averaged over time, the consumption of DO from the diffusive boundary layer and regeneration of DO levels by turbulent eddies result in a mean exchange rate, described by the DO difference across the diffusive boundary layer and a mass transfer coefficient, known as the gas transfer velocity ( $k$ ) (e.g., Lorke et al., 2003; Lorke & Peeters, 2006). Therefore, the thickness of the BBL, the characteristic time and length scales of turbulent eddies, and other associated turbulent statistics are routinely used as controlling parameters to determine the gas transfer velocity at the SWI (e.g., Brand et al., 2009; Bryant et al., 2010; Lorke & Peeters, 2006). Similar processes also occur at the air-water interface, and Lorke and Peeters (2006) suggested a unified scaling relation for gas transfer velocity at both interfaces using law-of-the-wall scaling, hypothesizing that  $k$  is dependent on  $u_*$ . The validity of this relation at the SWI under the influence of bubble plumes is tested in this paper.

The present study is a continuation of a previous effort to understand the impact of bubble plume flow rate on the spatial and temporal variability of sediment oxygen uptake in two oxygenated lakes (Bierlein et al., 2017). Bierlein et al. (2017) focused on fine-scale measurements of DO near and through the SWI of these lakes and discussed the increased sediment DO flux due to hypolimnetic oxygenation. The measurements employed a diverse group of sensors under well-controlled oxygenation conditions in two stratified lakes, allowing us to evaluate the lake dynamics, the structure of the BBL turbulence, and the influence of oxygenation bubble plumes on gas transfer at the SWI. This is important to understand the fate of oxygen supplied to lakes by oxygenation bubble plumes and to help optimize oxygen injection to achieve efficient restoration of hypolimnetic waters.

In this paper, we elucidate the effects of bubble plumes on near- and far-field dynamics of a stratified lake using temperature, velocity, and DO measurements in the water column. Velocity measurements included two acoustic Doppler velocimeters (ADV) and a high-resolution acoustic Doppler current profiler (ADCP). From the velocity data, we examine the near-bed turbulence in low-energy lakes and evaluate the influence of bubble plume oxygenation. Particularly, we evaluate the validity of the law-of-the-wall in quantifying the BBL velocity profiles and determine whether the bubble plume causes unconventional parameterization of near-bed flow and turbulence. Combining turbulence analyses with the DO flux measurements in Bierlein et al. (2017), we extend observations of the relation between  $k$  and  $u_*$  proposed in Lorke and Peeters (2006) toward the lower end of  $u_*$  by one order of magnitude. We also examine the scales of turbulent eddies and interfacial renewal time as a further assessment of the mechanisms determining the turbulence control over the DO flux in the BBL of oxygenated lakes. The scope of this paper is limited to understanding the physical processes, whereas chemical and biological factors (e.g., redox processes) of DO dynamics are not discussed here.

This paper is organized as follows. In Section 2, we introduce two study sites, describe their oxygenation systems, and present the methods used to measure BBL turbulence using ADVs and ADCPs. The results of the measurements and their discussion are followed in Section 3. These include flow statistics in the hypolimnion of both lakes under different, controlled oxygenation settings, thermal structure and the spectra of temperature and velocity, velocity profiles and turbulence in the lake BBL, and the turbulence mechanisms responsible for gas transfer at the SWI. Finally, Section 4 summarizes the conclusions.

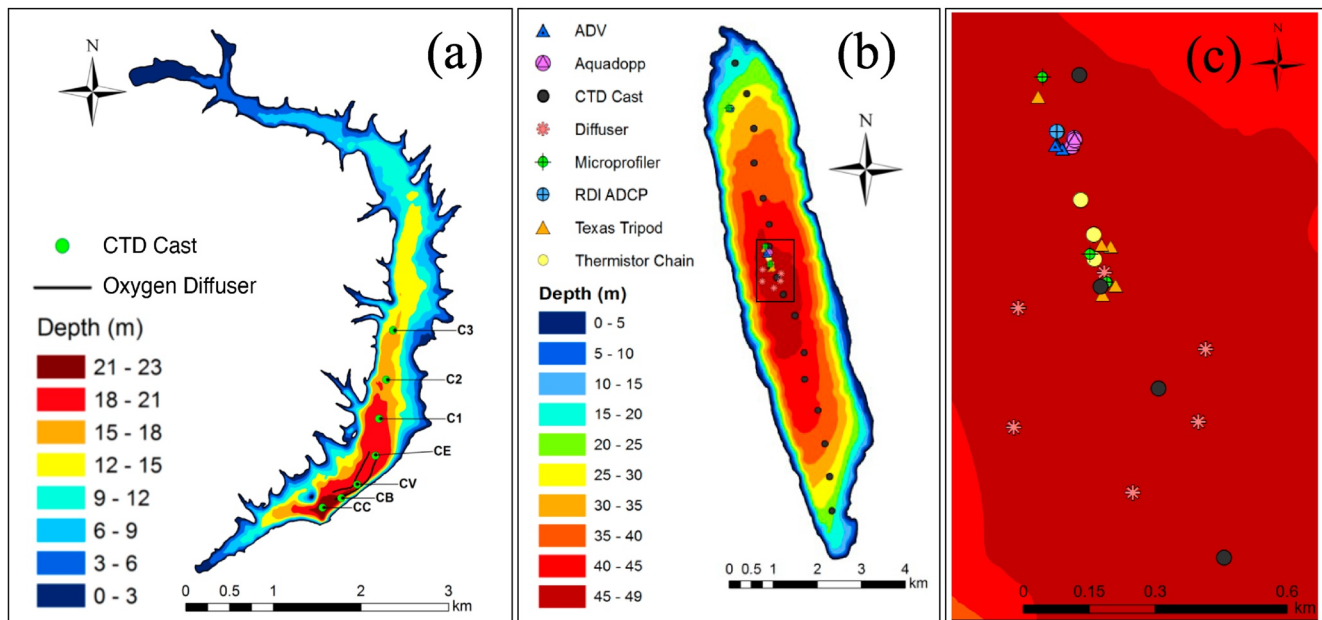


**Figure 1.** Bathymetry data of the two study lakes and the locations of instrument deployments and oxygenation diffusers. (a) Carvins Cove Reservoir; (b) Lake Hallwil (LH); (c) Zoom-in view of the instruments around the diffusers in LH (the black box in (b)).

## 2. Methods

### 2.1. Sites Description

Two field campaigns were conducted in two moderately deep (>20 m) inland water bodies. The first campaign was carried out during 14 May to 1 June 2012 in Lake Hallwil (LH), which is located in the Canton of Aargau, Switzerland (47°16'51.2" N, 8°13'02.8" E; Figures 1b and 1c). The second campaign was carried out during 26 May to 2 June 2013 in Carvins Cove Reservoir (CCR), which is located in the State of Virginia, U.S. (37°23'19.2"N, 79°56'54.3"W; Figure 1a). Both water bodies are eutrophic, dimictic, and have weak inflows. Seasonal anoxia was reported in LH; whereas, CCR maintains relatively better DO levels according to available data (Doubek et al., 2018; Holzner et al., 2012). Oxygenation is used to counter the low hypolimnetic DO level during the summer stratification in both lakes. Figure 1 shows the bathymetric map of each system, the locations where various instruments were deployed, the locations of conductivity, temperature, and depth (CTD) measurements (i.e., CTD casts), and the location of the oxygenation diffusers. During both campaigns, the lakes exhibited clear stratification, which is observed from the measured temperature data (Figure 2).

### 2.2. Oxygenation Systems

Carvins Cove Reservoir has two, line-source oxygen diffusers, each about 750 m long, located in the deepest region of the lake, at the southern bank near the dam (Figure 1a). Lake Hallwil has six 6.5 m-diameter, circular diffusers, located in a circular pattern with a 300 m diameter ring in the deepest part of the lake near the centroid of the area (Figures 1b and 1c) (McGinnis et al., 2004). During the experiments, the diffusers were operated at different flow rates each day. The time-varying gas flow rates were adjusted with pre-defined on-duty and off-duty durations (Figure 3).

### 2.3. Measurements

DO concentration at the SWI and the DO fluxes were measured at both sites using an in situ oxygen micro-profiler (Bierlein et al., 2017). The micro-profiler measures DO concentration at 1 Hz frequency within a spatial region between 10 mm below the SWI and 100 mm above the SWI. The vertical resolution is up to 0.1 mm within 5 mm distance from the SWI on both sides. The DO fluxes across the SWI were estimated from measured profiles of DO concentration using Fick's law (Bryant et al., 2011). The details of DO measurements and data analysis can

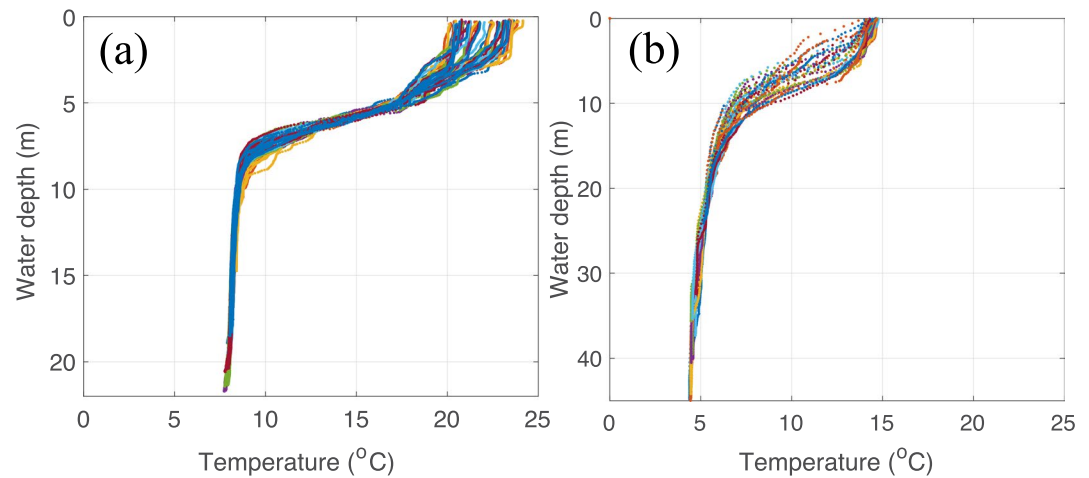


**Figure 2.** Temperature profiles in the two study lakes measured using conductivity, temperature, and depth (CTD) casts. Carvins Cove Reservoir was sampled from 26 May to 2 June 2013 (a). Lake Hallwil was sampled from 14 May to 1 June 2012 (b). Different colors show different CTD casts made during the experimental campaigns. The locations of CTD casts are marked in Figure 1.

be found in Bierlein et al. (2017). At the same time as DO measurements, the turbulence in the BBL of each lake was measured using one or two ADVs (Nortek Vector) and a high-resolution ADCP (Nortek Aquadopp Profiler, 1 MHz), mounted on bottom platforms close to the micro-profiler. The ADVs recorded continuous measurements at a sample rate of 8 Hz, which is adequate to resolve the smallest turbulent time scales (see later Table 3). The sample volumes of the ADVs were positioned about 15 cm above the SWI. The ADCP was mounted in a down-looking configuration at a height of approximately 1.5 m above the sediments. The ADCP measured the BBL turbulence at a sample rate of 4 Hz using a burst configuration (512-s burst of data collection followed by a 1,288-s interval of downtime).

CTD casts and thermistor chains were deployed in the two study lakes to monitor the thermal structure in the water column. These measurements showed strong stratification in both lakes (Figure 2). Periodic variation of

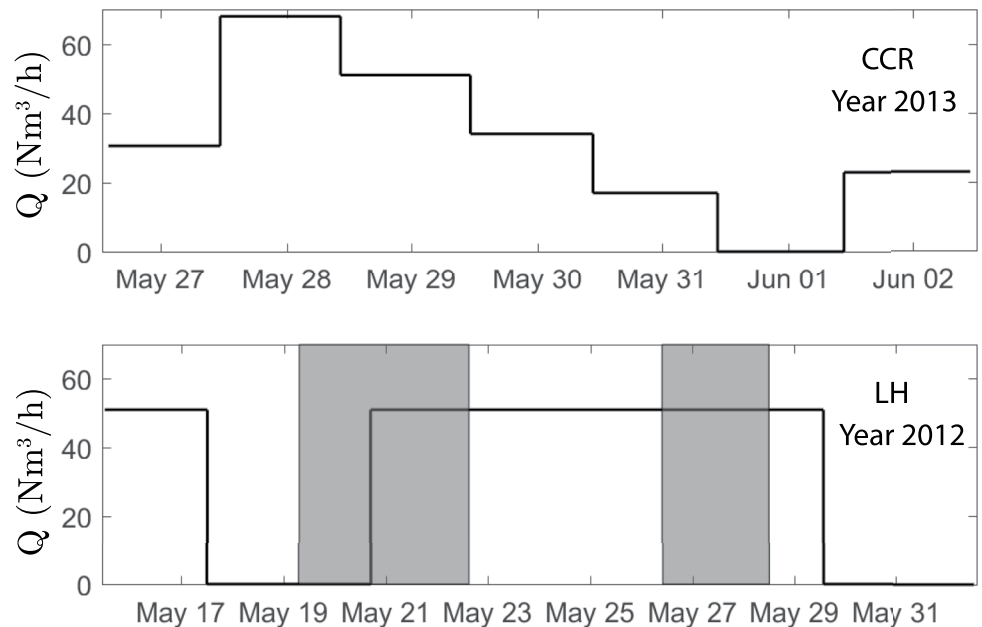


**Figure 3.** Time series of gas flow rates for the oxygenation diffusers at the two study sites in the unit of normal cubic meter per hour. The velocity measurements were conducted at all times when diffusers were operating, except for the period indicated by the shaded areas at the Lake Hallwil site. CCR: Carvins Cove Reservoir; LH: Lake Hallwil.

temperature at mid-water depths was observed, which is likely due to internal motion that responded to changes in the gas flow rates as the buoyant forcing provided by the plumes changed. The DO sensor on the CTD also provided vertical distributions of the DO concentration in the lakes during the experiments. A weather station was also deployed at each experiment site and recorded ambient conditions such as wind speed, air temperature, and precipitation.

### 3. Results and Discussion

#### 3.1. Large-Scale Lake Dynamics

##### 3.1.1. Near-Bed Velocity Statistics

The measurements from the ADVs and ADCP show good agreement on the variation of velocity magnitudes and directions (Figures S1 and S2 in Supporting Information S1). Very weak velocities were present during the experiments in both lakes (Figure 4). The majority of the velocity magnitudes from the ADCP at 1 m above the bottom (mab) (>90% of the data) were smaller than 2 cm/s in both lakes. Lake Hallwil had a slightly broader current speed distribution, with about 23% of current speeds >1 cm/s; whereas, CCR had 15% of observed currents >1 cm/s (Figures 4a and 4b). Velocity data show oscillating currents in both lakes, and the major flow directions were aligned with the long-axis of the lakes at the measurement locations (Figures 4c and 4d, see also Figure S3 in Supporting Information S1).

##### 3.1.2. Lake Dynamics Parameters

The meteorologic data and several bulk lake parameters summarize the atmospheric forcing and lake conditions during the experiments (Table 1). Wind data from the weather station were analyzed to characterize the atmospheric boundary layer over the lake.  $U_{10}$  is the wind speed at 10 m height. The wind shear velocity on the water side is computed as  $u_{*sw} = (\rho_a C_D U_{10}^2 / \rho_w)^{1/2}$ , where  $\rho_a$  is the density of air,  $\rho_w$  is the density of water, and  $C_D = 1.3 \cdot 10^{-3}$  is drag coefficient (Smith & Banke, 1975). From the ADCP measurement, we report the mean water flow  $\overline{U}_{1m}$  at 1 mab. We also report  $u_{*b}$ , the median friction velocity in the BBL measured with the ADCPs. In Table 1, we define the bulk Reynolds number as  $Re = \overline{U}_{1m} z_{1m} / \nu$ , where  $\nu = 1 \cdot 10^{-6} \text{ m}^2/\text{s}$  is the kinematic viscosity of water,  $z_{1m} = 1 \text{ m}$  indicates 1 m above the lake bottom,  $\overline{U}_{1m}$  is the averaged velocity at  $z_{1m}$ . The period of the barotropic seiche ( $T_{seiche,0}$ ) is estimated using both the Merian formula and the three-layer method (Münich et al., 1992). Both methods yield similar values, within a 10% difference, and the results of the three-layer method are reported. The period of the first mode of internal lake seiche ( $T_{seiche,1}$ ) is computed after Mortimer (1952) as  $2L_0 / \sqrt{g(\rho_h - \rho_e)/(\rho_h/h_h + \rho_e/h_e)}$ , where  $L_0$  is length of the lake;  $g$  is gravitational acceleration;  $\rho_h$  and  $\rho_e$  are the water densities in the hypolimnion and epilimnion;  $h_h$  and  $h_e$  are the hypolimnion and epilimnion thicknesses. These scales are used in the following sections to help interpret the fine-scale observations.

##### 3.1.3. Effect of Bubble Plume on Near- and Far-Field Dynamics

The buoyant plume caused by the oxygenation lifted cold and low DO water from the near-bed region into the water column (Figure 5). The water column temperature and DO were obtained from 32 CTD casts within 40 m distance, centered at the diffuser ring. In the near-field of the bubble plume, the thermal stratification was disrupted as a result of strong vertical mixing induced by the plume entrainment. The measured upwelling flow represents a “snapshot” around the bubble plume determined by the path of CTD casts, which does not show a symmetric feature about the ring center. However, in the far-field of the bubble plume on the lake-scale, the upward movement of water was compensated by a returning, downwelling flow. The returning flow had a much larger spatial scale, which may be attributed to the interactions between the plume-induced flow and the internal seiching (McGinnis et al., 2004). In this case, the oxygenated lake showed a depression of the isotherms with persistent warmer water at greater depths in most of the lake when the diffusers were operational (Figures 6a and 6b). Only the near-field of the bubble plume showed isotherms deflected upward. After the diffusers were turned off, oscillations were initiated by removal of the buoyant force of the oxygenation, and the thermal structure gradually restored to its natural stratification (Figures 6c and 6d).

##### 3.1.4. Spectra of Velocity and Temperature

Spectral analysis of the ADV data illustrates the dynamics of the large-scale motions that were sensed near the bottom (Figures 7a and 7b). The spectrum was calculated for the velocity of the entire period of observation



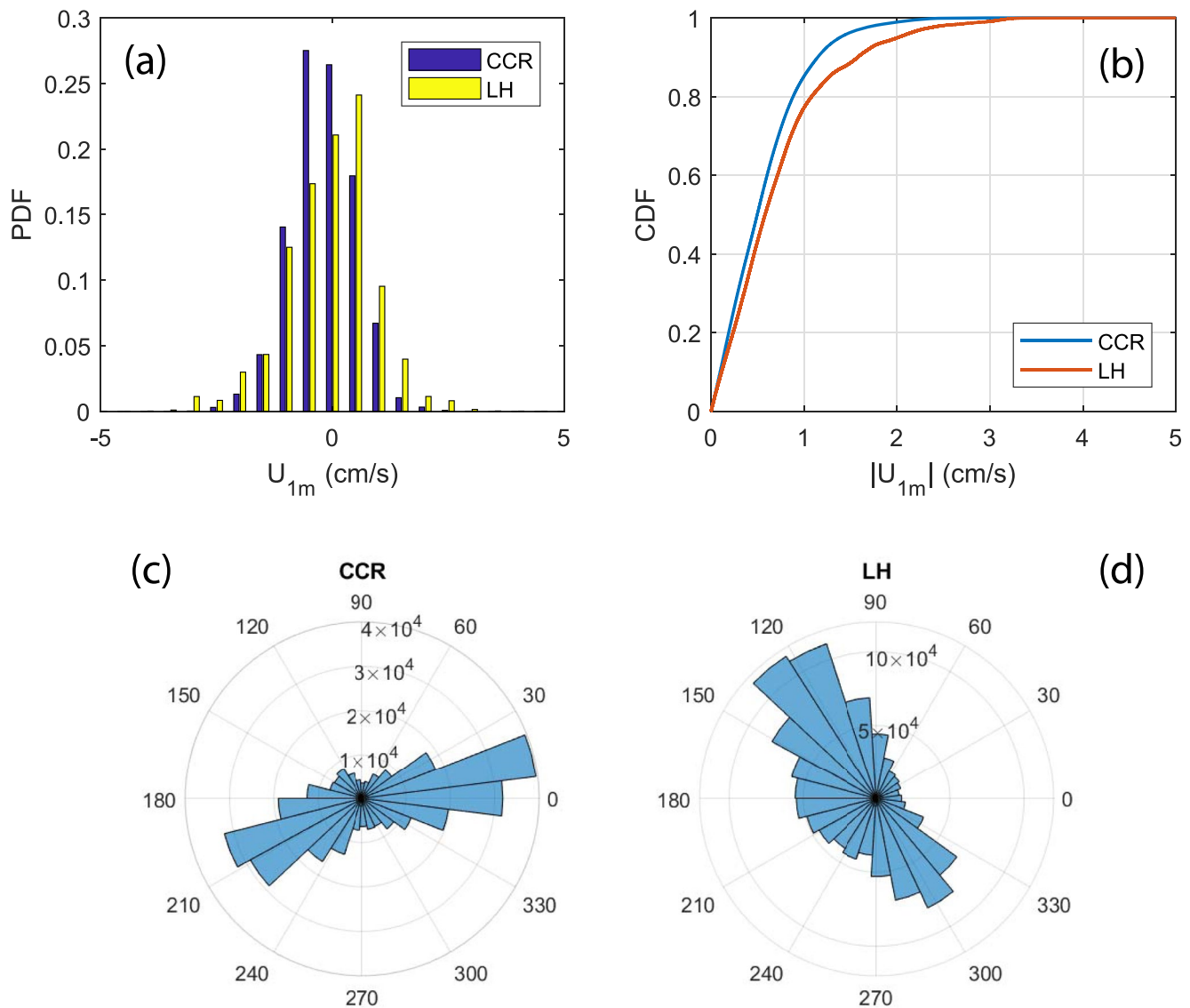


**Figure 4.** Statistics of the bottom boundary layer currents from the acoustic Doppler current profiler in the two study lakes during the field campaigns (26 May to 2 June 2013 for Carvins Cove Reservoir; 14–19 May, 22–26 May, and 28 May to 1 June 2012 for Lake Hallwil): (a and b) probability density function and cumulative distribution function of the flow speeds at 1 m above the bottom (mab). (c and d) Polar-histogram of flow directions at 1 mab.

in CCR; whereas, the spectrum for LH was calculated for the second period of velocity measurements, after the diffuser had been operated at steady-state for three days (23–26 May 2012; Figure 3). The spectrum was smoothed by applying a Gaussian filter at the cut-off window of the Kolmogorov time scale and by averaging sections of the velocity record that had a window size of 10% of the total record length and applying a 50% overlap between each averaging window. In the spectra data, a well-defined inertial subrange across at least two orders of magnitude in the frequency domain can be observed in both lakes, showing the Kolmogorov scaling, that is,

**Table 1**  
Parameters of the Two Study Sites Analyzed From the Measurements

	$\bar{U}_{10}$ [m/s]	$\bar{u}_{*stc}$ [cm/s]	$\bar{U}_{1m}$ [cm/s]	$\bar{u}_{*b}$ [cm/s]	Re [–]	$h_h$ [m]	$h_e$ [m]	$\rho_h$ [kg/m <sup>3</sup> ]	$\rho_e$ [kg/m <sup>3</sup> ]	$T_{seiche,0}$ [min]	$T_{seiche,1}$ [hr]
Carvins Cove Reservoir	2.80	0.35	0.85	0.044	8,500	11	3	999.9	997.8	14	13.3
Lake Hallwil	6.17	0.77	1.12	0.18	11,200	30	3	1,000.1	999.3	13	38

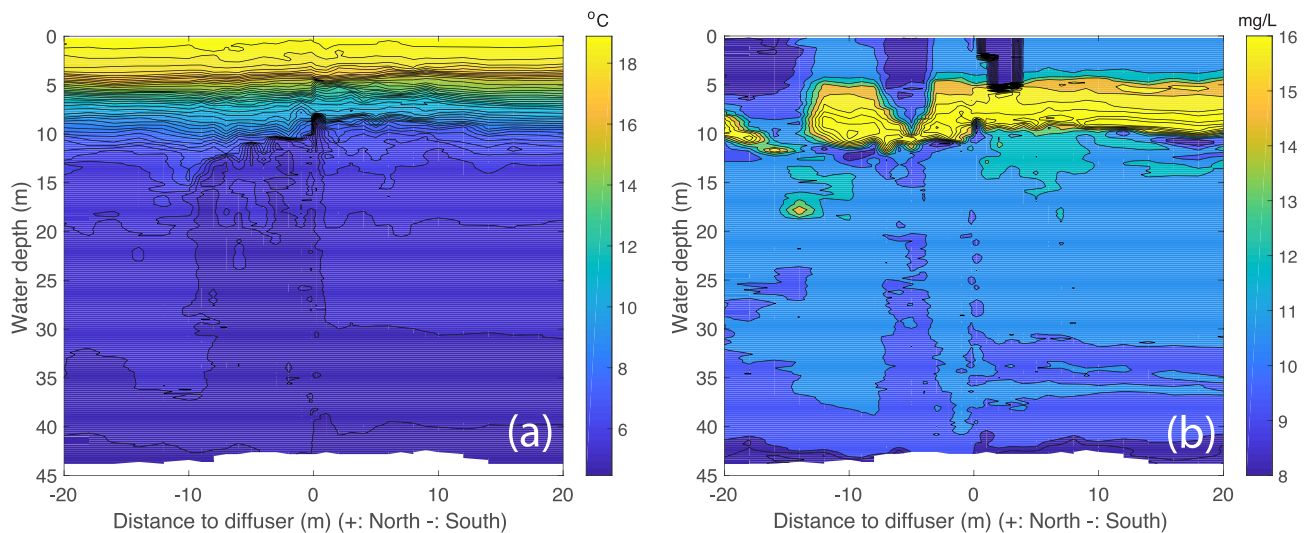


**Figure 5.** Map of temperature and dissolved oxygen (DO) in the near-field region of one of the bubble plumes in Lake Hallwil. Data were obtained from conductivity, temperature, and depth transect measurements on 30 May 2012 close to one ring of diffusers. (a) Temperature; (b) DO concentration. Zero on the  $x$ -axis is centered on one of the 6.5 m-diameter diffuser rings.

a universal  $-5/3$  spectral slope. The low frequency bound of this  $-5/3$  region occurs around  $10^3$  cycles per day (cpd), which is equivalent to  $\sim 90$  s. This is about 6 and 29 times the Kolmogorov scale in CCR and LH, respectively. This criterion satisfies the definition of an inertial subrange. The Kolmogorov scale in the inertial subrange will be later used for estimating dissipation rates of TKE. Both spectra exhibit multiple peaks, indicating several modes of internal wave motions in the lakes that resulted in oscillatory motion within the BBL.

The calculated periods of the barotropic seiche mode (Table 1) agree well with the peaks observed in the velocity spectra (14 min for CCR and 13 min for LH; Figure 7). The 13 min oscillation in LH was also reported in velocity spectra during June and September of 2001 (Gwaze, 2003). Using the three-layer method, the first-order internal seiche mode in both the horizontal and vertical directions was calculated to be 10.5 hr for CCR and 14.5 hr in LH. The Mortimer (1952) equation for internal wave dynamics, which does not use the thickness of the metalimnion, gives a period of 13.3 hr for CCR and 38 hr in LH. If these longer periods were present, their signatures were eclipsed by noise and other peaks in the spectra, which may be due to the operation of the diffusers during these experimental campaigns. For example, the influence of the diffusers is observed in the spectrum data in CCR, where the change of flow rate was made periodically at 24 hr intervals, yielding a subtle peak at 1 cpd in the velocity spectrum for CCR (Figure 7a).

Temperature spectra also show a respectable  $-5/3$  subrange (Figures 7c and 7d). Peaks in the spectra for the sensors located in the thermocline region may indicate the time scales of interactions between the bubble plume and the internal wave dynamics. However, the quantitative relationship between basin-scale motions and the bubble plume operations remains unclear and is subject to future studies.

### 3.2. Bottom Boundary Structure

#### 3.2.1. Velocity Profiles

We evaluate the bottom shear and the structure of the BBL at both study sites using all of the velocity data, irrespective of the different oxygen flow rates of the bubble plume diffusers. The probability density function of the velocity (Figure 4) and low-frequency peaks in the velocity spectra (Figure 7) indicate that the BBL flows are oscillatory, with oscillation frequencies corresponding to basin-scale barotropic and baroclinic wave modes. Thus, these velocity data elucidate the flow structure of an oscillating BBL that is primarily induced by lake internal wave motion.

The velocity data show that the main flow oscillations having changes in the direction of the velocity generally occurred at seiche periods of 10–20 hr. This corresponds to a Stokes layer thickness  $\delta_s = \sqrt{2\nu/\omega}$  of 0.1–0.15 m,

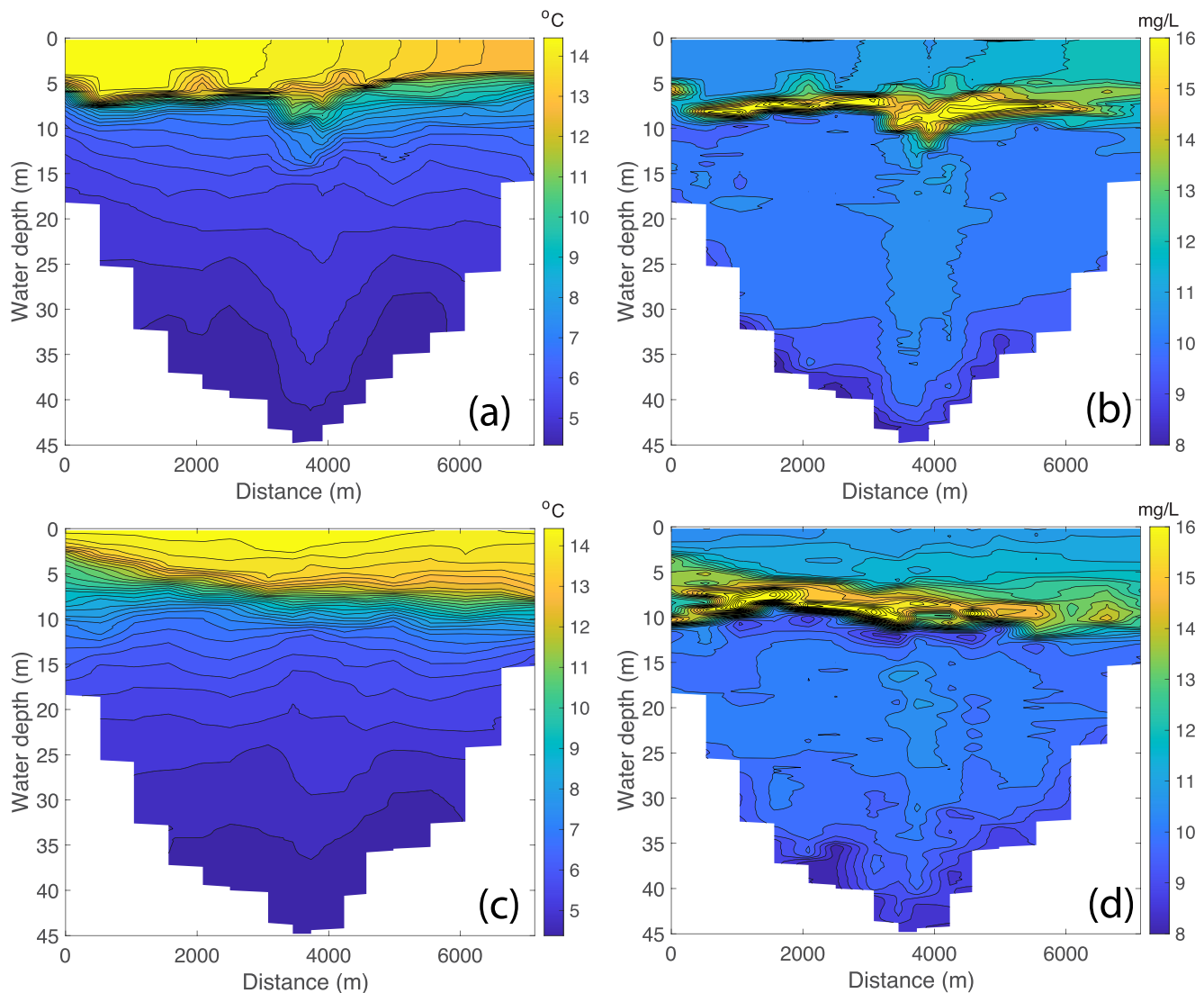


**Figure 6.** Map of temperature and dissolved oxygen (DO) concentration at Lake Hallwil. Data were obtained from the conductivity, temperature, and depth (CTD) measurements across the lake, where the locations of CTD casts are shown in Figure 1. The diffusers are located in the deepest area of the lake. (a) Temperature and (b) DO were measured on 16 May 2012 when the diffusers were operational. (c) Temperature and (d) DO were measured on 19 May 2012 when the diffusers were not operational.

where  $\nu$  is the kinematic viscosity of water and  $\omega$  is the angular frequency (Spalart & Baldwin, 1989). Hence, the Reynolds number defined for an oscillatory boundary layer flow can be estimated as  $Re = \delta_s U_{0m} / \nu \approx 2,000 - 3,000$  using the free-stream maximum velocity magnitude  $U_{0m} = 1.5 - 2$  cm/s estimated from the 90th-percentile of the cumulative distribution function of the velocity magnitude. Therefore, the oscillating boundary layer flow presented in this study is likely within the fully developed turbulence regime, that is, turbulence is present during most of the oscillating cycle (Jabbari & Boegman, 2021).

Lorke et al. (2002) show that a logarithmic fit to the velocity profile starting from 0.5 m above the SWI would lead to overestimation of bottom shear and roughness in the oscillating BBL. That being said, the canonical law-of-the-wall is not valid in an oscillatory BBL because it is strictly for stationary shear induced flows. Lorke et al. (2002) suggest that the law-of-the-wall is likely valid in the lowest 0.5 m, depending on the modification of the oscillatory currents to the stationary shear. The validity of the logarithmic velocity profile in a short vertical region of the oscillating boundary layer is also shown in other studies (Jensen et al., 1989), especially within the fully developed turbulence regime (Jabbari & Boegman, 2021). To examine the velocity profiles obtained here using the law-of-the-wall scaling and its modification, we fit logarithmic profiles to the profiles of mean



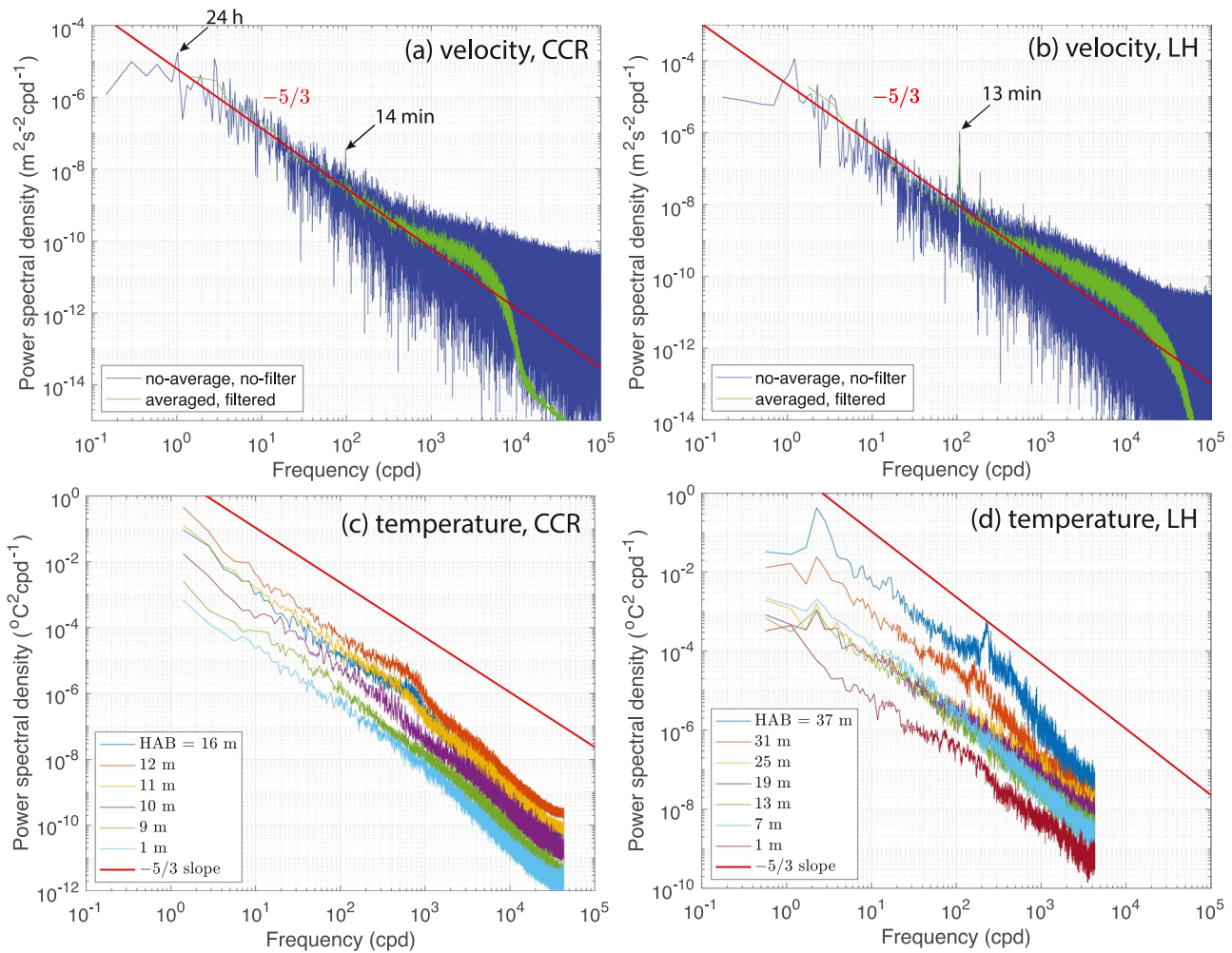


**Figure 7.** Spectrum of the longitudinal velocity component measured from the acoustic Doppler velocimeters and the temperature from the thermistor chain: (a) velocity, CCR; (b) velocity, Lake Hallwil (LH). “No-average, no-filter” represents the spectrum of the entire time series of the velocity data; “averaged, filtered” represents the averaged spectrum of velocity data sections with a 10% window size at a 50% overlap, and filtered with a Gaussian filter. (c) Temperature, CCR; (d) temperature, LH. Spectra were averaged with a 10% window size at a 50% overlap similar to the velocity spectra. “HAB” in the legend indicates thermistor locations as height above bottom.

velocities over each data burst from the down-looking ADCP. Several sequential steps were carried out for this process. First, we defined a coordinate system with the  $x$ -axis being the main flow (longitudinal) direction, such that the mean velocity on its perpendicular direction ( $y$ -axis; transverse) is zero. We found that the logarithmic profiles held from the SWI to 0.4 mab in both lakes, and the flows became less organized above 0.4 mab. Given that the law-of-the-wall was only found to apply within the lowest region of our velocity profiles, logarithmic fits were only performed to the bottom 0.4 m of the velocity profiles  $U(z)$ , where  $U$  is the burst-average velocity in the  $x$ -direction. Second, we applied the law-of-the-wall fitting to the measured data using the classical profile

$$U(z) = \frac{u_*}{\kappa} \ln\left(\frac{z}{z_0}\right) \quad (1)$$

where  $z_0$  is the roughness height; we take the von Kármán constant  $\kappa$  as 0.41. Fitting this canonical profile to the data yielded the fit parameters  $u_*$  and  $z_0$ . Third, log-linear profiles were fitted to the same data using the profile

$$U(z) = \frac{u_*}{\kappa} \left[ \ln\left(\frac{z}{z_0}\right) + \frac{z}{L} \right] \quad (2)$$

where  $u_*$  and the length scale  $L$  were fitting parameters, keeping  $z_0$  fixed and equal to the previously found value based on fitting the canonical law-of-the-wall profile. The length scale  $L$  depends on modifications of

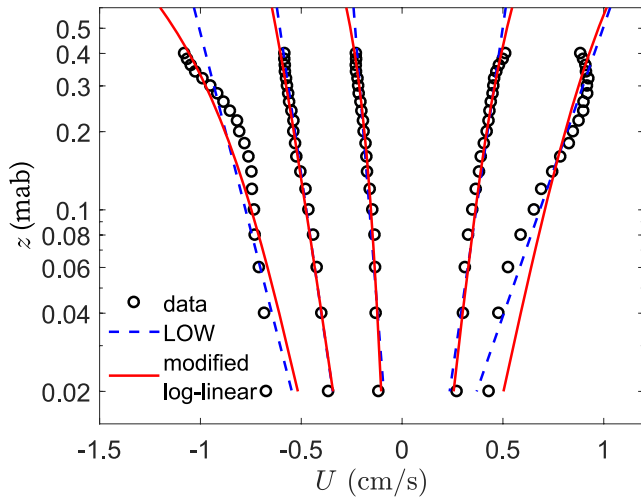


**Figure 8.** An example of two logarithmic fits to the oscillating flow in the bottom boundary layer of Carvins Cove Reservoir. Data shown here span 17.5 hr during 29–30 May 2013. LOW is the law-of-the-wall scaling, given in Equation 1; the modified log-linear profile is that defined by Equation 2.

the profile, with positive values for flow deceleration and negative values for flow acceleration (Lueck & Lu, 1997). The modified log-linear profile fits the BBL structure better in low-energy deep lakes, where flows tend to be more unsteady, that is, containing more accelerating/decelerating events (Cannon & Troy, 2018; Troy et al., 2016). Figure 8 shows an example of applying these logarithmic fits to the oscillatory flow observed in the BBL of CCR. Similar results were observed in LH (not shown).

### 3.2.2. Drag Coefficient

The shear velocities obtained from the logarithmic fits define the bottom shear stress  $\tau_0 = \rho_w u_*^2$ . We used a quadratic-law drag correlation between  $\tau_0$  and the burst-average velocities measured at 1 mab,  $U_{1m}$ , and obtained the drag coefficient ( $C_{1m}$ ) from the regressions fit to

$$u_* = C_{1m}^{1/2} U_{1m} \quad (3)$$

Results for each lake are shown in Figure 9. Although the flows deviate from the law-of-the-wall scaling above 0.4 mab,  $U_{1m}$  is still a good representative outer-layer forcing responsible for generating the bottom shear stress. Here, we choose  $U_{1m}$  to allow us to compare to previously reported values in other lakes using this scale. We found that  $u_*$ -values obtained from fitting both the canonical law-of-the-wall and the modified log-linear relations result

in strong correlation between  $U_{1m}$  and  $u_*$ , where the modified log-linear fit gives a better correlation than the law-of-the-wall.  $C_{1m}$  were found to be 0.0027 in CCR and 0.0085 in LH. If we use the  $u_*$ -values obtained from the law-of-the-wall fitting,  $C_{1m}$  were found to be 0.0018 and 0.0088 in CCR and LH, respectively.  $C_{1m}$  in CCR is comparable to the values reported in the literature for similar weak flow environments; whereas  $C_{1m}$  in LH is higher than values reported in other deep lakes. For example, for large, deep lakes, the literature reports 0.0023 in Lake Baikal (Ravens et al., 2000), 0.002 ~ 0.003 in Lake Superior (Churchill et al., 2004), 0.0044 in Lake Michigan (Cannon & Troy, 2018; Troy et al., 2016), 0.0042 ~ 0.0048 in Lake Erie (Valipour et al., 2015). Lorke et al. (2002) used classic law-of-the-wall scaling and calculated  $C_{1m} = 0.009$  in a similar weak oscillatory boundary in Lake Alpnach, a lake much more similar in depth and size to LH. Lorke et al. (2002) attributed the large  $C_{1m}$  values to the invalidity of the law-of-the-wall scaling as the oscillation compressed the turbulent bottom layer and thereby increased the apparent drag coefficient.

Typically, different drag coefficients are due to different bottom substrate, as the bottom roughness can increase the drag coefficient in the BBL (Davis & Monismith, 2011; Reidenbach et al., 2006). The range of drag coefficients can also be affected by the performance of logarithmic fitting. In oscillating flows, the correlation between

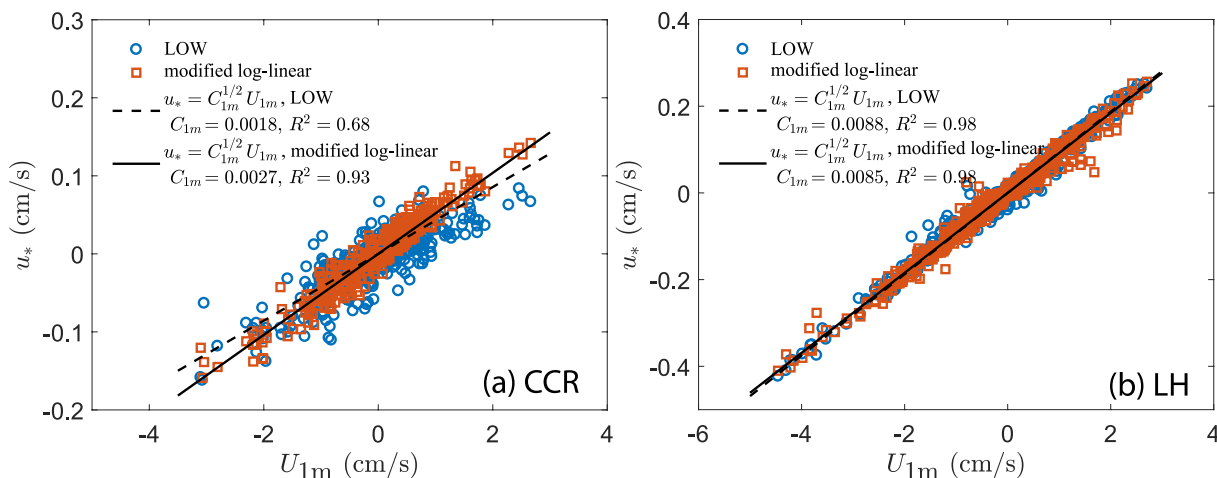


**Figure 9.** Correlation between shear velocities ( $u_*$ ) and the burst-mean velocities at 1 mab ( $U_{1m}$ ). The drag coefficients ( $C_{1m}$ ) were calculated from the regressions.

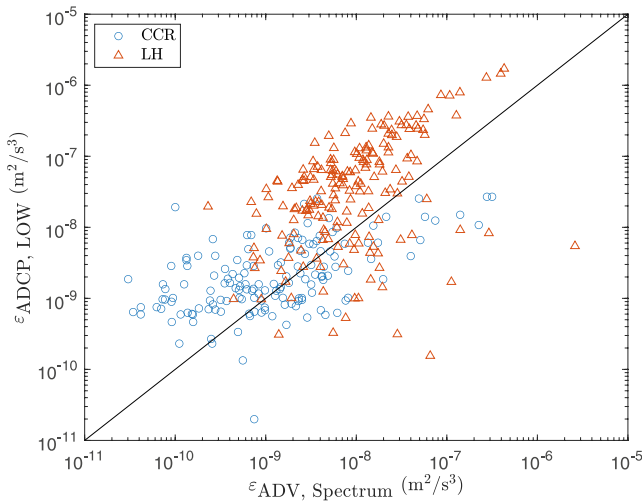


**Figure 10.** Comparison of estimates of the turbulent kinetic energy dissipation rates from the velocity measurements of the acoustic Doppler current profiler, using law-of-the-wall scaling, and the acoustic Doppler velocimeter, using fitting of the velocity spectra. Each data point represents 512-s burst duration of the velocity measurement.

the velocity at 1 m and the logarithmic velocity structure in the lowest 0.4 m may be different from that for stationary shear flows. Interestingly, the large values of  $C_{1m}$  were only found in LH; whereas, the oscillatory flows in CCR do not lead to large drag coefficients. With the present data, it is unclear what is responsible for this difference in drag coefficient. The bubble-plume induced flow may play a role, but a definitive cause requires further study.

### 3.2.3. Dissipation Rate of Turbulent Kinetic Energy

The dissipation rate of TKE ( $\epsilon$ ) was estimated using two independent methods, each applied to different instruments. For the ADCP data, we estimated  $\epsilon$  directly from  $\epsilon_{LOW} = u_*^3/(\kappa z)$  using  $u_*$  from logarithmic fitting to the burst-averaged velocity profiles. For the ADV data, we compute  $\epsilon$  by fitting to the velocity spectra in the well-defined inertial subrange (Bryant et al., 2010; Wang & Liao, 2016). The relationship between  $\epsilon$  and the one-dimensional energy spectrum in the inertial subrange follows (Pope, 2000):

$$E_{ii}(k_1) = \alpha_i \epsilon^{2/3} k_1^{-5/3} \quad (4)$$

where  $E_{ii}$  is the spectrum of each velocity component as a function of the wavenumber in the main flow direction ( $k_1$ ) with  $i = 1, 2, 3$  denoting the spectral estimation using velocity in the  $x$ -,  $y$ -, and  $z$ -directions. Coefficients  $\alpha_1 = 1.56 \times 18/55$  and  $\alpha_2 = \alpha_3 = 4\alpha_1/3$  (Polzin et al., 2021). The time series velocity data obtained by the ADV were used to calculate energy spectra

in the frequency domain  $E_{ii}(f)$ , which were then converted to spectra in the wave number domain by invoking Taylor's frozen-turbulence hypothesis:  $E_{ii}(k_1) = \frac{U}{2\pi} E_{ii}(f)$  with  $k_1 = \frac{2\pi}{U} f$ .

In order to have a direct comparison between these methods, we evaluate the law-of-the-wall scaling for the ADCP at the same height  $z$  as the sample volume of the ADV. The velocity spectra for the ADV data was computed over the same burst periods as measured by the ADCP. The inertial subrange fitting of the ADV data was applied to the spectra of both the longitudinal ( $x$ -direction) and transverse ( $y$ -direction) velocity components, and the average values were used as the final result:  $\epsilon_{ADV} = 0.5 \left( \left( E_{11} k_1^{5/3} / \alpha_1 \right)^{3/2} + \left( E_{22} k_1^{5/3} / \alpha_2 \right)^{3/2} \right)$ . The turbulent fluctuations of the vertical velocity component were suppressed due to the close proximity to the bottom, yielding an unobservable inertial subrange in  $E_{33}$ ; hence, the  $w$  velocity component was not used for this analysis. The spectral fittings with  $R^2$ -values  $< 0.7$  were rejected, concluding that the inertial subrange was not observed in those cases. These unsuccessful fittings typically occurred when the flow was too weak to be considered as turbulent. For the successful fittings, the Taylor's frozen-turbulence hypothesis was validated by examining the mean flow velocity, which was consistently at least an order of magnitude greater than the turbulent fluctuations. The direct comparison of the two estimates of  $\epsilon$  in each data burst is shown in Figure 10 and the time series of  $\epsilon$  are given in the supplementary file (Figure S4 in Supporting Information S1).

In both lakes, the two methods have a good agreement on the order of magnitude of  $\epsilon$ , with considerable scatter among individual estimates. In LH, values of  $\epsilon$  from the law-of-the-wall estimates are generally larger than those estimated using the spectral fitting. This may be attributed to the observed large drag coefficients in LH based on the law-of-the-wall profile of velocities. Lorke et al. (2002) suggests  $u_*$  can be overestimated by a factor of 1.5 when roughness height and drag coefficient are overestimated by a factor of 5 in weak oscillatory flows. If the drag coefficient in LH was overestimated by a factor of 3–5,  $u_*$  may be overestimated by a factor of  $\sim 1.5$ . This would lead to an overestimation of  $\epsilon$  using the law-of-the-wall scaling by a factor of  $1.5^3 \approx 3.4$ . Our data show  $\epsilon_{LOW}/\epsilon_{ADV} = 6.8$ , which is the same order of magnitude as this estimated factor. Note that even without factoring, the agreement between the two methods is within the general uncertainty of  $\epsilon$  estimates, on the order of  $10^{-8} \text{ m}^2/\text{s}^3$ . Values of  $\epsilon$  in LH were about two to three times larger than those in CCR (Table 2).

The flow oscillation alternates between acceleration and deceleration, which typically results in enhanced and suppressed turbulence in comparison to that in a stationary shear boundary layer (Yang & Lee, 2007). Such flow structures would disrupt the traditional turbulence mechanism and result in an imbalance in TKE production and dissipation during flow acceleration and deceleration. However, the flow is still shear dominant. Therefore, the

**Table 2**  
*Estimated Turbulent Kinetic Energy Dissipation Rates From Different Instruments Using Different Methods*

Site	Instrument	Method	TKE dissipation rate ( $\text{m}^2/\text{s}^3$ )	
			Mean	Standard deviation
Carvins Cove Reservoir	ADV	Spectrum	$3.8 \times 10^{-9}$	$8.6 \times 10^{-9}$
	ADCP	Law-of-the-wall	$1.1 \times 10^{-8}$	$4.2 \times 10^{-8}$
Lake Hallwil	ADV	Spectrum	$3.2 \times 10^{-8}$	$1.9 \times 10^{-7}$
	ADCP	Law-of-the-wall	$4.5 \times 10^{-8}$	$1.2 \times 10^{-7}$

modification of turbulence should be shown as data scattering around the structure of stationary shear flows. This is evidenced by generally balanced turbulence shear production and dissipation rate with considerable scattering in both lakes (Figure S5 in Supporting Information S1). Two orders of magnitude variations of TKE were also found in both lakes as a result of flow oscillation (Figure S6 in Supporting Information S1).

### 3.3. DO Transfer Across the Sediment-Water Interface

Time series data of the DO transfer process at the SWI are examined to elucidate the relationship between gas transfer and the combined effects of bubble plume operations and near-bottom turbulence (Figures 11 and 12). The interfacial DO flux ( $J$ ) was computed directly from the micro-profiler data. The DO in the bulk water ( $C_{\text{bulk}}$ ) and at the SWI ( $C_{\text{swi}}$ ) were measured by the micro-profiler. The gas transfer velocity ( $k$ ) was calculated using  $k = J/(C_{\text{bulk}} - C_{\text{swi}})$ . The TKE dissipation rate ( $\epsilon$ ) was obtained from the ADV data and raised to the quarter power. The shear velocity ( $u_*$ ) was determined by fitting the logarithmic velocity profile in the bottom 0.4 m and also computed using Equation 3 with measured  $U_{1m}$ .

In CCR (Figure 11), the oxygenation plume flow rate was changed daily, reaching a peak flow rate on 28 May and being turned off on June 1. The bulk DO had a mean value of  $162 \text{ mmol}/\text{m}^3$  and a standard deviation of  $20 \text{ mmol}/\text{m}^3$  over the whole span of the experiment. A gradual decrease of DO concentration in the bulk water was observed as the flow rate of the oxygenation system decreased. The DO concentration at the SWI was always less than that in the bulk water, with a mean value of  $72 \text{ mmol}/\text{m}^3$  and a standard deviation of  $27 \text{ mmol}/\text{m}^3$ . Hence, during the entire experiment, the lake sediment was an DO sink, and the flux of DO into the sediments was mostly controlled by the stronger variation of DO at the SWI than by variation in the bulk water.

The gas transfer velocity, a turbulence-controlled parameter, was plotted along with the TKE dissipation rate to the power of  $1/4$  (Figure 11), where  $k \sim \epsilon^{1/4}$  represents the small-eddy model of the interfacial gas transfer process (Lamont & Scott, 1970; Wang et al., 2015; Zappa et al., 2007). The data show that  $k$  was not correlated with  $\epsilon$  in the first two to three days but had much better correlation after 29 May when the gas flow rate started to decrease. Similar correlation is observed between  $k$  and  $u_*$ . The time series of  $u_*$  show similar variations as  $\epsilon^{1/4}$ . The linear relation between  $k$  and  $u_*$  is an alternative gas transfer model in shear dominant diffusive boundary layers (Lorke & Peeters, 2006).

In LH (Figure 12), the bubble plumes were switched on and off, and the gas flow rate was constant while the diffusers were in operation. Similar to CCR, the sediment in LH was always a sink of DO; however, both  $C_{\text{bulk}}$  and  $C_{\text{swi}}$  changed more than in CCR. The variation of  $C_{\text{bulk}}$  and  $C_{\text{swi}}$  have a similar tendency, which is likely due to the dynamics of patches of water with variable DO concentration being advected over the measurement location. During the first half of the experiment, the bulk water had a predominantly low DO. The concentration abruptly increased around 25 May and remained elevated through the remainder of the experiment. The fairly uniform bulk concentration during these two different periods suggests a fairly well-mixed condition at the measurement site.  $C_{\text{swi}}$  shows much greater variability than the concentration in the bulk water, indicating that mass transfer is controlled at the SWI.

Given the larger change of DO, the variability of DO flux in LH (mean =  $8.4 \text{ mmol}/\text{m}^2\text{d}$ , standard deviation =  $5.2 \text{ mmol}/\text{m}^2\text{d}$ ) is larger than that in CCR (mean =  $5.0 \text{ mmol}/\text{m}^2\text{d}$ , standard deviation =  $1.7 \text{ mmol}/\text{m}^2\text{d}$ ). With the strong variability in the DO fluxes, the direct correlation between  $k$  and  $\epsilon$  is not clearly observed (Figure 12). The relative independence of  $k$  and  $\epsilon$  in the time series data may be due to weak turbulence, where



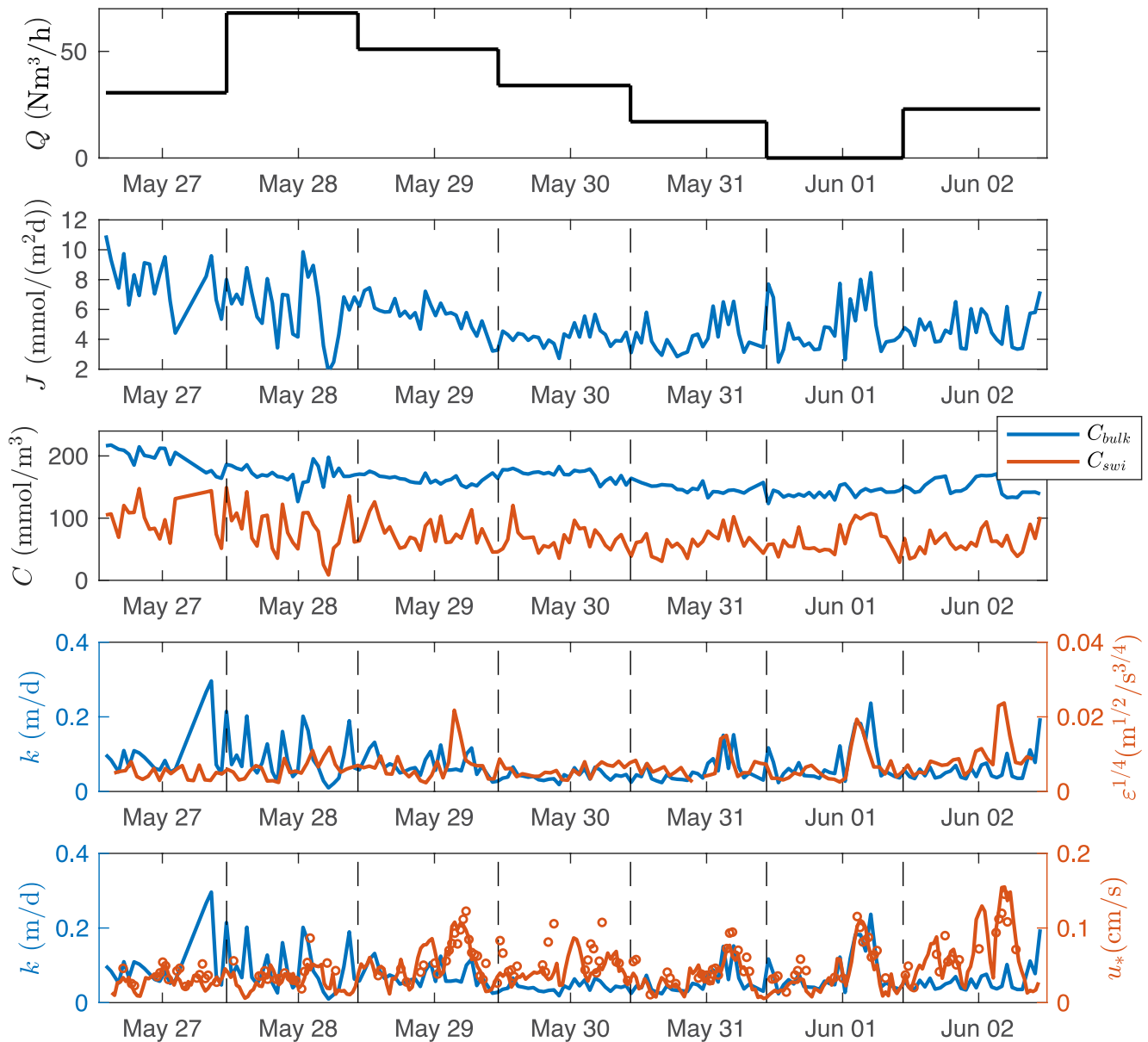


**Figure 11.** Time series for Carvins Cove Reservoir:  $Q$ —gas flow rate of the oxygenation bubble plume;  $J$ —dissolved oxygen (DO) flux computed directly from the micro-profiler at the SWI;  $C_{bulk}$ —DO concentration in bulk water at the top of the profile measured with micro-profiler;  $C_{swi}$ —DO concentration measured at the SWI;  $k$ —gas transfer velocity;  $\varepsilon$ —dissipation rate of turbulent kinetic energy computed from acoustic Doppler velocimeter data;  $u_*$ —shear velocity: circles represent those estimated from the law-of-the-wall fitting to the velocity profiles, solid line represents those calculated from Equation 3.

the time and length scales that control the gas transfer do not correlate with those that are responsible for the turbulent dissipation, known as small-scale processes. Larger scale dynamics may also be important in the sediment DO flux processes when the turbulent Reynolds number becomes small for weak flows (Chu & Jirka, 1992; Theofanous et al., 1976).  $u_*$  shows a slightly better correlation with  $k$ , but the correlation is still weak.

Given the relatively weak correlation between  $k$  and  $u_*$  in the time series data, we evaluate both parameters over the entire measurement period (Figure 13). Lorke and Peeters (2006) provided a relation  $k = Sc^{-1/2} u_* / 9$  for boundary layers at both air-water and SWIs following the law-of-the-wall scaling, where  $Sc = \nu/D$  is the Schmidt number and  $D$  is the molecular diffusivity, here of oxygen, taken as  $1.88 \cdot 10^{-9} \text{ m}^2/\text{s}$ . This form of the mass transfer velocity scale is identical to the small-eddy model with the dominant diffusive length scale being the Batchelor scale defined by  $L_B = 2\pi(\nu D^2/\varepsilon)^{1/4}$  (Lorke & Peeters, 2006). We plot our observations together with those



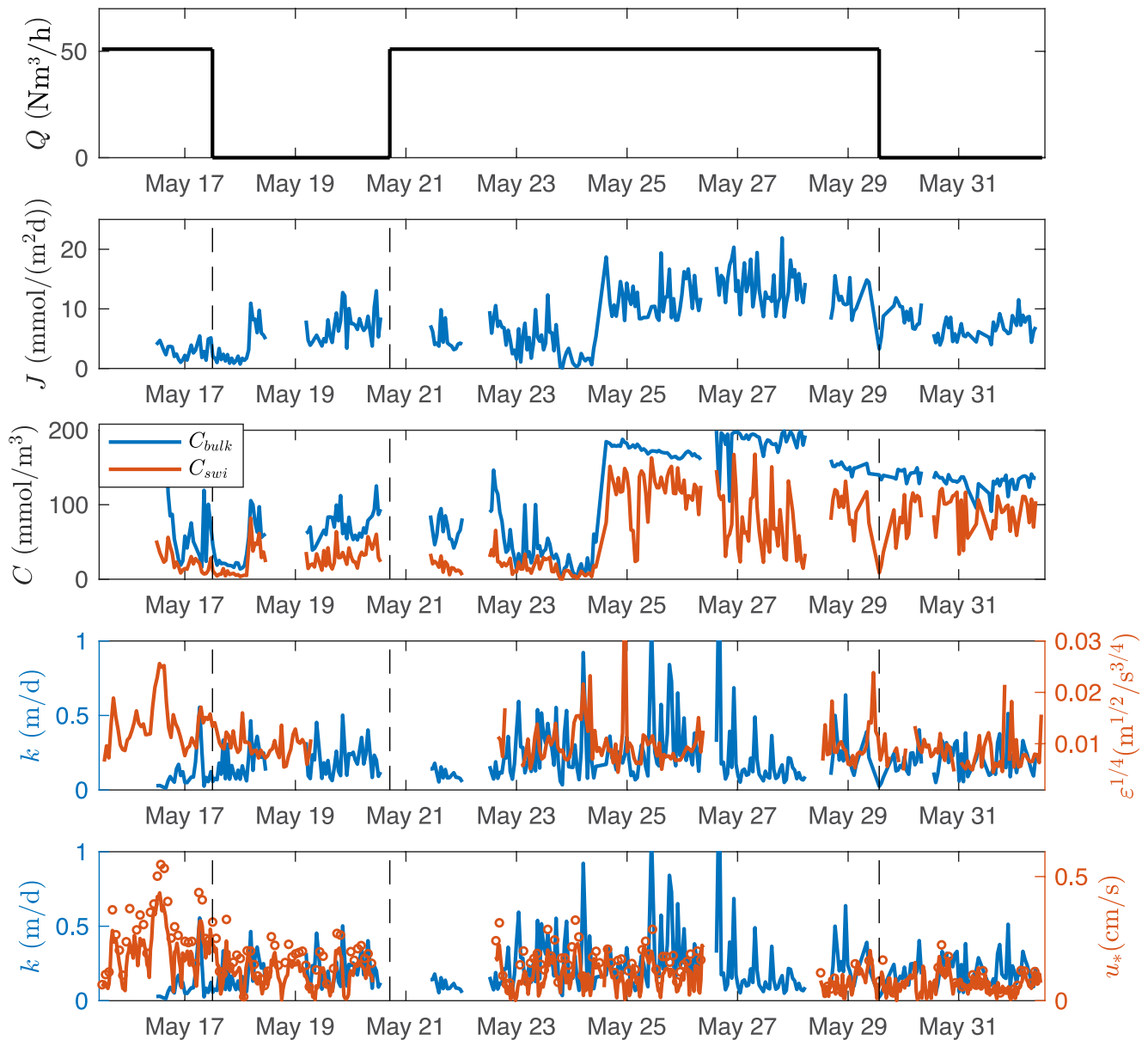


**Figure 12.** Time series for Lake Hallwil. See Figure 11 for explanation of variables. Only one-third of shear velocity data collected are shown (circles in the lowest subplot) for those estimated from the velocity profile fitting.

from the literature reported by Lorke and Peeters (2006) (Figure 13). The mean and standard deviation of the data in each lake are plotted using points and errorbars, respectively. Our measurement data extend the scaling to an order of magnitude smaller values of  $u_*$ . Our data also confirm the relationship in Lorke and Peeters (2006) at even smaller, less energetic scales. This suggests that turbulent structure and diffusivity at the Batchelor scale are the dominant mechanisms controlling mass transfer at the SWI. However, the weak dependence between  $k$  and  $u_*$  in the time series data (Figures 11 and 12) suggests the time scale of gas transfer velocity may be different from that responsible for the shear velocity. This is similar to the observed weak correlation between  $k$  and  $\varepsilon$  in the time series data. The diffusive boundary layer thickness is found to be close to the Ozmidov scale ( $l_o = \sqrt{\varepsilon/N^3}$ , where  $\varepsilon$  and buoyancy frequency  $N$  are evaluated at the height of the ADV measurements), which can be interpreted as the largest horizontal scale that has sufficient kinetic energy to overturn in the stratified environment. The measured data and analysis suggest that the gas transfer mechanism in low energetic environments may be influenced by multiple scaling factors, in contrast to the universal, small-eddy scaling in strong turbulent flows (Zappa et al., 2007).

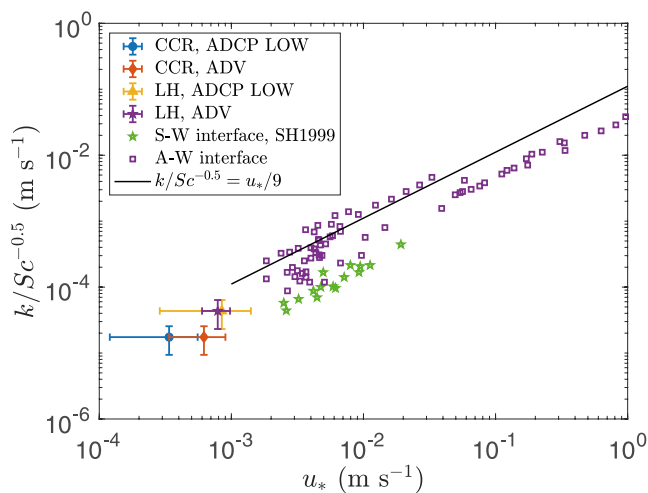


**Figure 13.** Gas transfer velocity as a function of friction velocity. “CCR” is Carvins Cove Reservoir; “LH” is Lake Hallwil; “ADCP LOW” denotes that  $u_*$  is estimated by fitting the law-of-the-wall scaling from the velocity profiles measured using acoustic Doppler current profiler. “ADV” denotes that  $u_*$  is estimated using  $u_* = \sqrt{-u'w'}$  from the acoustic Doppler velocimeter data. The data point and errorbars represent the mean and standard deviation of corresponding parameters in each lake. Literature data were reproduced from Figure 2 in Lorke and Peeters (2006). The literature data are grouped into two categories: sediment-water (S–W) interface and air-water (A–W) interface. “SH1999” is Steinberger and Hondzo (1999).

observed weak correlation between  $k$  and  $\epsilon$  or  $u_*$  in the time series data, as the time scales in burst-averaged data are inadequate to capture the variation of the gas transfer velocity caused by the large-scale turbulent motions which occur on time scales greater than those captured during each measurement burst. Apart from the physical mechanisms presented here, biotic processes and abiotic chemical reactions also affect the DO flux across the SWI including fauna respiration, bioirrigation, and redox transitions (Corzo et al., 2018; Jørgensen et al., 2022; Snelgrove et al., 2018). However, evaluation of the influences of these factors is out of scope of this paper and, hence, not discussed here.

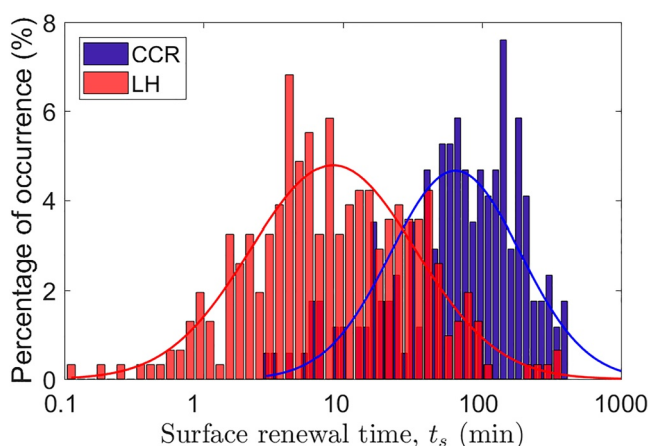


**Figure 14.** Distribution of surface renewal time on log-scale. The two solid lines represent the log-normal fit to the calculated surface renewal time.

To quantify the dominant time scales that are responsible for the DO flux at the sediment surface, we calculated the surface renewal time directly from the measured  $k$ :  $t_s = D/k^2$ . The percentage of occurrence of the renewal times in both lakes are shown in Figure 14. We observe a substantial range of renewal time scales, spanning more than two orders of magnitude within each lake and nearly four orders of magnitude across our study. The log-normal distribution fits fairly well with the renewal time in both lakes, with a mean value of  $\sim 100$  min in CCR and  $\sim 20$  min in LH (Table 3). The log-normal distribution of surface renewal time scales found in our data agrees with the turbulence-controlled interfacial transfer processes (e.g., heat flux on the ocean surfaces, Garbe et al., 2004).

To compare the surface renewal time scale of DO transfer with the turbulence time scales in the BBL, in Table 3, we summarize the characteristic length and time scales of near-bottom turbulence calculated from the ADV and ADCP measurements. By direct comparison between the diffusive boundary layer thickness ( $\delta_D$ ) and various turbulent length scales, we found that  $\delta_D$  is comparable to the Batchelor scale, though somewhat larger. This agrees with the Lorke and Peeters (2006) argument that the micro-scale of a passive scalar tracer provides the smallest length scale of turbulent tracer fluctuations, that is, the length scale that is dominant under Fickian diffusion for controlling mass transfer at the SWI. At the same time, we found the renewal time scale was statistically consistent with the largest time scale, the integral time scale calculated from the velocity auto correlation function, despite the very large range of individual surface renewal time scales. This suggests that the large energy-containing eddies are important to the interfacial transfer of DO at the SWI in weak flow conditions. This mechanism also explains the

## 4. Conclusions

In this paper, we investigate the mean flow, turbulence dissipation rate, and DO transfer across the SWI in the BBL of two deep lakes under operation of oxygenation bubble plumes. The bubble plumes were found to impact the dynamics of the lakes, including alteration of the frequencies of internal motion, which showed correlation with the frequencies of changes in operation of the bubble plume, creation of vertical flow circulation in the near-fields of the bubble plumes, and modulation of the time scales of the large-scale eddies. The effect of the bubble plume on the large-scale lake dynamics depends on the gas flow rate and duration of the bubble plume steady-state operation as well as the stratification and geometry of the lake (i.e., area, depth, shape). However, although the near-field of the bubble plumes were strongly impacted by the flow induced by the oxygenation bubbles, the bubble plume impact on the turbulent structure within the BBL in these deep, low-energy lakes was limited. Internal motions yielded slowly oscillating BBL, but the long time scales allowed the BBL turbulence to exhibit shear-dominated, quasi-steady structures.

Within the lowest 0.4 m, a logarithmic relationship was found to describe the mean velocity profiles, whereas the mean velocity profiles above 0.4 m

**Table 3**  
*Characteristic Scales of Turbulence and Sediment-Water Dissolved Oxygen Fluxes*

	Carvins Cove Reservoir				Lake Hallwil			
	ADV	ADCP	Micro-profiler	ADV	ADCP	Micro-profiler		
Length scale (cm)								
Kolmogorov $l_K = 2\pi(\nu/\epsilon)^{1/4}$	2.3 ± 1.0	1.9 ± 0.7	–	1.0 ± 0.3	0.7 ± 0.4	–		
Batchelor $l_B = 2\pi(\sqrt{D^2/\epsilon})^{1/4}$	0.10 ± 0.04	0.08 ± 0.03	–	0.04 ± 0.01	0.03 ± 0.02	–		
Integral $l_I = c_\mu \text{TKE}^{3/2}/\epsilon$	76 ± 131	10 ± 29 <sup>a</sup>	–	48 ± 58	14 ± 292 <sup>a</sup>	–		
Integral $l_I = U_{\text{ADV}} \int \text{ACF}(t) dt$	2,960 ± 1,380	–	–	2,750 ± 1,260	–	–		
Ozmidov $l_o = \sqrt{\epsilon/N^3}$	0.3 ± 0.5	0.5 ± 1.1	–	0.2 ± 0.5	0.2 ± 0.4	–		
Diffusive boundary layer $\delta_D = D/k = D\Delta C/I$	–	–	0.3 ± 0.2	–	–	–	0.13 ± 0.12	
	Carvins Cove Reservoir				Lake Hallwil			
Time scale (s)	ADV	ADCP	Micro-profiler	ADV	ADCP	Micro-profiler		
Kolmogorov $t_K = (\nu/\epsilon)^{1/2}$	15 ± 13	11 ± 9	–	3.0 ± 2.0	1.8 ± 3.6	–		
Batchelor $t_B = t_K$	15 ± 13	11 ± 9	–	3.0 ± 2.0	1.8 ± 3.6	–		
Integral $t_I = l_I/(2\text{TKE})^{1/2}$	228 ± 369	47 ± 144 <sup>a</sup>	–	49 ± 59	22 ± 434 <sup>a</sup>	–		
Integral $t_I = \int \text{ACF}(t) dt$	4,390 ± 2,050	–	–	3,770 ± 1,730	–	–		
Surface renewal $t_s = D/k^2 = D\Delta C^2/I^2$	–	–	6,030 (160 ~ 25,000)	–	–	1,260 (6 ~ 22,700)		
<i>Note.</i> The equations for calculating each parameter are given in the table. The length scale of energy-containing eddies was calculated using the $k$ - $\epsilon$ model and auto correlation function (ACF) methods. In the $k$ - $\epsilon$ model, the coefficient $c_\mu$ was taken as 0.09. In the ACF method, the integral range of the ACF was determined by the time of the first zero-crossing in the cross-correlation function. The dissipation rates used in the calculation of scales were reported in Table 2. Note: surface renewal time is reported as mean and range. All others are reported as mean and standard deviation.								

deviated from the canonical logarithmic scaling laws. A relatively high drag coefficient was found in LH, similar to values reported in previous studies. Lower drag coefficients typical of deep lakes were observed in Carvins Cove. Independent methodologies using spectral fitting in the inertial subrange and the law-of-the-wall scaling provide satisfactory estimations of turbulent dissipation rates close to the SWI, though with considerable scatter. These flow characteristics indicate shear-dominant flow structures in the BBL, and the substantial variations in the data elucidate the non-stationary dynamics.

The substantial changes in DO flux across the SWI are the result of DO concentration changes in the water column and at the SWI due to injection of oxygen into the system, that is, the main driving force of elevated DO fluxes. In addition, the gas transfer velocity follows a turbulence-controlled mechanism dominated by eddies having large time scales. In these two lakes, the thickness of the diffusive boundary layer is consistent with the turbulent Batchelor scale. The quasi-steady structure of the shear flow within the bottom 0.4 m above the SWI explains the observation that the corresponding friction velocities correlate to the gas transfer velocity. The variation of the observed surface renewal times in the concentration boundary layer fit to a log-normal distribution, and the observed times are statistically consistent with the integral time scale of turbulent eddies in both lakes. This is also consistent with the fact that we observed weak correlation between gas transfer velocity and the shear velocity or turbulent dissipation observed for individual data bursts, which were too short to capture the steady impact of these large time scale eddies. Hence, for these low-energy, deep lakes, the large energy-containing eddies appear to dominate the dynamics of DO flux at the SWI.

## Conflict of Interest

The authors declare no conflicts of interest relevant to this study.

## Data Availability Statement

The data used in this paper are available in the data repository (Wang et al., 2023).

## Acknowledgments

This research was supported in part by a grant from the U.S. National Science Foundation (CBET 1033514). We would also like to thank the Western Virginia Water Authority for access to and Kanton Aargau for access to Lake Hallwil during the field campaigns. We also thank Michi Schurter of Eawag, Arno Stöckli of Kanton Aargau, and Christina Urbanczyk for their valuable assistance during the field campaigns.

## References

- Beutel, M. W., & Horne, A. J. (1999). A review of the effects of hypolimnetic oxygenation on lake and reservoir water quality. *Lake and Reservoir Management*, 15(4), 285–297. <https://doi.org/10.1080/07438149909354124>
- Bierlein, K. A., Rezvani, M., Socolofsky, S. A., Bryant, L. D., Wüest, A., & Little, J. C. (2017). Increased sediment oxygen flux in lakes and reservoirs: The impact of hypolimnetic oxygenation. *Water Resources Research*, 53(6), 4876–4890. <https://doi.org/10.1002/2016WR019850>
- Brand, A., Dinkel, C., & Wehrli, B. (2009). Influence of the diffusive boundary layer on solute dynamics in the sediments of a Seiche-driven lake: A model study. *Journal of Geophysical Research*, 114(G1), G01010. <https://doi.org/10.1029/2008JG000755>
- Bryant, L. D., Hsu-Kim, H., Gantzer, P. A., & Little, J. C. (2011). Solving the problem at the source: Controlling Mn release at the sediment-water interface via hypolimnetic oxygenation. *Water Research*, 45(19), 6381–6392. <https://doi.org/10.1016/j.watres.2011.09.030>
- Bryant, L. D., Lorrain, C., McGinnis, D. F., Brand, A., Wüest, A., & Little, J. C. (2010). Variable sediment oxygen uptake in response to dynamic forcing. *Limnology & Oceanography*, 55(2), 950–964. <https://doi.org/10.4319/lo.2010.55.2.0950>
- Cannon, D. J., & Troy, C. D. (2018). Observations of turbulence and mean flow in the low-energy hypolimnetic boundary layer of a large lake. *Limnology & Oceanography*, 63(6), 2762–2776. <https://doi.org/10.1002/lno.11007>
- Chu, C. R., & Jirka, G. H. (1992). Turbulent gas flux measurements below the air-water interface of a grid-stirred tank. *International Journal of Heat and Mass Transfer*, 35(8), 1957–1968. [https://doi.org/10.1016/0017-9310\(92\)90198-2](https://doi.org/10.1016/0017-9310(92)90198-2)
- Churchill, J. H., Williams, A. J., & Ralph, E. A. (2004). Bottom stress generation and sediment transport over the shelf and slope off of Lake Superior's Keweenaw Peninsula. *Journal of Geophysical Research*, 109, C10S04–C10. <https://doi.org/10.1029/2003JC001997>
- Corzo, A., Jiménez-Arias, J., Torres, E., García-Robledo, E., Lara, M., & Papaspyrou, S. (2018). Biogeochemical changes at the sediment–water interface during redox transitions in an acidic reservoir: Exchange of protons, acidity and electron donors and acceptors. *Biogeochemistry*, 139(3), 241–260. <https://doi.org/10.1007/s10533-018-0465-7>
- Davis, K. A., & Monismith, S. G. (2011). The modification of bottom boundary layer turbulence and mixing by internal waves shoaling on a barrier reef. *Journal of Physical Oceanography*, 41(11), 2223–2241. <https://doi.org/10.1175/2011JPO4344.1>
- Doubek, J. P., Campbell, K. L., Doubek, K. M., Hamre, K. D., Lofton, M. E., McClure, R. P., et al. (2018). The effects of hypolimnetic anoxia on the diel vertical migration of freshwater crustacean zooplankton. *Ecosphere*, 9(7), e02332. <https://doi.org/10.1002/ecs2.2332>
- Garbe, C. S., Schimpf, U., & Jähne, B. (2004). A surface renewal model to analyze infrared image sequences of the ocean surface for the study of air-sea heat and gas exchange. *Journal of Geophysical Research*, 109(C8), C08S15. <https://doi.org/10.1029/2003JC001802>
- Gwaze, S. (2003). *Structure, dynamics and energetics of internal waves in Lake Hallwil*. Master's thesis. UNESCO-IHE Inst. for Water Educ.
- Holzner, C. P., Tomonaga, Y., Stöckli, A., Denecke, N., & Kipfer, R. (2012). Using noble gases to analyze the efficiency of artificial aeration in Lake Hallwil, Switzerland. *Water Resources Research*, 48(9), W09531. <https://doi.org/10.1029/2012WR012030>
- Jabbari, A., & Boegman, L. (2021). Parameterization of oscillating boundary layers in lakes and coastal oceans. *Ocean Modelling*, 160, 101780. <https://doi.org/10.1016/j.ocemod.2021.101780>
- Jensen, B. L., Sumer, B. M., & Fredsøe, J. (1989). Turbulent oscillatory boundary layers at high Reynolds numbers. *Journal of Fluid Mechanics*, 206, 265–297. <https://doi.org/10.1017/S0022112089002302>

- Jørgensen, B. B., Wenzhöfer, F., Egger, M., & Glud, R. N. (2022). Sediment oxygen consumption: Role in the global marine carbon cycle. *Earth-Science Reviews*, 228, 103987. <https://doi.org/10.1016/j.earscirev.2022.103987>
- Lamont, J. C., & Scott, D. S. (1970). An eddy cell model of mass transfer into the surface of a turbulent liquid. *AIChE Journal*, 16(4), 513–519. <https://doi.org/10.1002/aic.690160403>
- Lorke, A., Müller, B., Maerki, M., & Wüest, A. (2003). Breathing sediments: The control of diffusive transport across the sediment—Water interface by periodic boundary-layer turbulence. *Limnology & Oceanography*, 48(6), 2077–2085. <https://doi.org/10.4319/lo.2003.48.6.2077>
- Lorke, A., & Peeters, F. (2006). Toward a unified scaling relation for interfacial fluxes. *Journal of Physical Oceanography*, 36(5), 955–961. <https://doi.org/10.1175/JPO2903.1>
- Lorke, A., Umlauf, L., Jonas, T., & Wüest, A. (2002). Dynamics of turbulence in low-speed oscillating bottom-boundary layers of stratified basins. *Environmental Fluid Mechanics*, 2(4), 291–313. <https://doi.org/10.1023/A:1020450729821>
- Lueck, R. G., & Lu, Y. (1997). The logarithmic layer in a tidal channel. *Continental Shelf Research*, 17(14), 1785–1801. [https://doi.org/10.1016/S0278-4343\(97\)00049-6](https://doi.org/10.1016/S0278-4343(97)00049-6)
- McGinnis, D. F., Lorke, A., Wüest, A., Stöckli, A., & Little, J. C. (2004). Interaction between a bubble plume and the near field in a stratified lake. *Water Resources Research*, 40(10), W10206. <https://doi.org/10.1029/2004WR003038>
- Mortimer, C. H. (1952). Water movements in lakes during summer stratification; evidence from the distribution of temperature in Windermere. *Philosophical Transactions of the Royal Society of London Series B Biological Sciences*, 236(635), 355–398. <https://doi.org/10.1098/rstb.1952.0005>
- Müller, B., Bryant, L. D., Matzinger, A., & Wüest, A. (2012). Hypolimnetic oxygen depletion in eutrophic lakes. *Environmental Science and Technology*, 46(18), 9964–9971. <https://doi.org/10.1021/es301422r>
- Münnich, C., Wüest, A., & Imboden, D. M. (1992). Observations of the second vertical mode of the internal seiche in an alpine lake. *Limnology & Oceanography*, 37(8), 1705–1719. <https://doi.org/10.4319/lo.1992.37.8.1705>
- Polzin, K. L., Wang, B., Wang, Z., Thwaites, F., & Williams, A. J. (2021). Moored flux and dissipation estimates from the northern deepwater Gulf of Mexico. *Fluid*, 6(7), 237. <https://doi.org/10.3390/fluids6070237>
- Pope, S. B. (2000). *Turbulent flows*. Cambridge University Press.
- Ravens, T. M., Kocsis, O., Wüest, A., & Granin, N. (2000). Small-scale turbulence and vertical mixing in Lake Baikal. *Limnology & Oceanography*, 45(1), 159–173. <https://doi.org/10.4319/lo.2000.45.1.0159>
- Reidenbach, M. A., Monismith, S. G., Koseff, J. R., Yahel, G., & Genin, A. (2006). Boundary layer turbulence and flow structure over a fringing coral reef. *Limnology & Oceanography*, 51(5), 1956–1968. <https://doi.org/10.4319/lo.2006.51.5.1956>
- Singleton, V. L., & Little, J. C. (2006). Designing hypolimnetic aeration and oxygenation systems - A review. *Environmental Science and Technology*, 40(24), 7512–7520. <https://doi.org/10.1021/es060069s>
- Smith, S. D., & Banke, E. G. (1975). Variation of the sea surface drag coefficient with wind speed. *Quarterly Journal of the Royal Meteorological Society*, 101(429), 665–673. <https://doi.org/10.1002/qj.49710142920>
- Snelgrove, P. V., Soetaert, K., Solan, M., Thrush, S., Wei, C.-L., Danovaro, R., et al. (2018). Global carbon cycling on a heterogeneous seafloor. *Trends in Ecology and Evolution*, 33(2), 96–105. <https://doi.org/10.1016/j.tree.2017.11.004>
- Spalart, P. R., & Baldwin, B. S. (1989). In J.-C. André, J. Cousteix, F. Durst, B. E. Launder, F. W. Schmidt, & J. H. Whitelaw (Eds.), *Direct simulation of a turbulent oscillating boundary layer, Turbulent shear flows* (Vol. 6, pp. 417–440). Springer Berlin Heidelberg.
- Steinberger, N., & Hondzo, M. (1999). Diffusional mass transfer at sediment-water interface. *Journal of Environmental Engineering*, 125(2), 192–200. [https://doi.org/10.1061/\(ASCE\)0733-9372\(1999\)125:2\(192\)](https://doi.org/10.1061/(ASCE)0733-9372(1999)125:2(192))
- Theofanous, T., Houze, R., & Brumfield, L. (1976). Turbulent mass transfer at free, gas-liquid interfaces, with applications to open-channel, bubble and jet flows. *International Journal of Heat and Mass Transfer*, 19(6), 613–624. [https://doi.org/10.1016/0017-9310\(76\)90044-2](https://doi.org/10.1016/0017-9310(76)90044-2)
- Troy, C., Cannon, D., Liao, Q., & Bootsma, H. (2016). Logarithmic velocity structure in the deep hypolimnetic waters of Lake Michigan. *Journal of Geophysical Research: Oceans*, 121(1), 949–965. <https://doi.org/10.1002/2014JC010506>
- Valipour, R., Bouffard, D., & Boegman, L. (2015). Parameterization of bottom mixed layer and logarithmic layer heights in central Lake Erie. *Journal of Great Lakes Research*, 41(3), 707–718. <https://doi.org/10.1016/j.jglr.2015.06.010>
- Wang, B., & Liao, Q. (2016). Field observations of turbulent dissipation rate profiles immediately below the air-water interface. *Journal of Geophysical Research-Oceans*, 121(6), 4377–4391. <https://doi.org/10.1002/2015JC011512>
- Wang, B., Liao, Q., Fillingham, J. H., & Bootsma, H. A. (2015). On the coefficients of small eddy and surface divergence models for the air-water gas transfer velocity. *Journal of Geophysical Research: Oceans*, 120(3), 2129–2146. <https://doi.org/10.1002/2014JC010253>
- Wang, B., Rezvani, M., Bierlein, K., Bryant, L., Little, J., Wüest, A., & Socolofsky, S. (2023). Dataset for ‘effects of bubble plumes on lake dynamics, near-bottom turbulence, and transfer of dissolved oxygen at the sediment-water interface’ [Dataset]. Zenodo. <https://doi.org/10.5281/zenodo.7561914>
- Wüest, A., Brooks, N. H., & Imboden, D. M. (1992). Bubble plume modeling for lake restoration. *Water Resources Research*, 28(12), 3235–3250. <https://doi.org/10.1029/92wr01681>
- Yang, S. Q., & Lee, J. W. (2007). Reynolds shear stress distributions in a gradually varied flow in a roughened channel. *Journal of Hydraulic Research*, 45(4), 462–471. <https://doi.org/10.1080/00221686.2007.9521780>
- Zappa, C. J., McGillis, W. R., Raymond, P. A., Edson, J. B., Hints, E. J., Zemmelen, H. J., et al. (2007). Environmental turbulent mixing controls on air-water gas exchange in marine and aquatic systems. *Geophysical Research Letters*, 34(10), L10601. <https://doi.org/10.1029/2006GL028790>